Article

Discriminating between Biotic and Abiotic Stress in Poplar Forests Using Hyperspectral and LiDAR Data

Quan Zhou [1], Jinjia Kuang [1], Linfeng Yu [1], Xudong Zhang [1], Lili Ren [1,2,*] and Youqing Luo [1,2]

1   Beijing Key Laboratory for Forest Pest Control, Beijing Forestry University, Beijing 100083, China;
    quan_z@bjfu.edu.cn (Q.Z.); kuang823249587@bjfu.edu.cn (J.K.); yulinfeng@ifrit.ac.cn (L.Y.);
    zhangxd@bjfu.edu.cn (X.Z.); yqluo@bjfu.edu.cn (Y.L.)
2   Sino-French Joint Laboratory for Invasive Forest Pests in Eurasia, Beijing Forestry University—French
    National Research Institute for Agriculture, Food and Environment (INRAE), Beijing 100083, China
*   Correspondence: lily_ren@bjfu.edu.cn

Abstract: Sustainable forest management faces challenges from various biotic and abiotic stresses. The Asian longhorned beetle (ALB) and drought stress both induce water shortages in poplar trees, but require different management strategies. In northwestern China, ALB and drought stress caused massive mortality in poplar shelterbelts, which seriously affected the ecological functions of poplars. Developing a large-scale detection method for discriminating them is crucial for applying targeted management. This study integrated UAV-hyperspectral and LiDAR data to distinguish between ALB and drought stress in poplars of China's Three-North Shelterbelt. These data were analyzed using a Partial Least Squares-Support Vector Machine (PLS-SVM). The results showed that the LiDAR metric (elev_sqrt_mean_sq) was key in detecting drought, while the hyperspectral band (R970) was key in ALB detection, underscoring the necessity of integrating both sensors. Detection of ALB in poplars improved when the poplars were well watered. The classification accuracy was 94.85% for distinguishing well-watered from water-deficient trees, and 80.81% for detecting ALB damage. Overall classification accuracy was 78.79% when classifying four stress types: healthy, only ALB affected, only drought affected, and combined stress of ALB and drought. The results demonstrate the effectiveness of UAV-hyperspectral and LiDAR data in distinguishing ALB and drought stress in poplar forests, which contribute to apply targeted treatments based on the specific stress in poplars in northwest China.

Keywords: hyperspectral image; LiDAR; Asian longhorned beetle; drought; poplar

1. Introduction

The Asian longhorned beetle (*Anoplophora glabripennis* Motschulsky [Coleoptera: Cerambycidae], ALB) is a wood-boring pest that poses a significant biotic threat to broadleaved forests worldwide [1]. Native to Eastern China and the Korean Peninsula, it is recognized as one of the 100 worst invasive alien species in the world by the International Union for Conservation of Nature (IUCN). The ALB was first intercepted in North America in 1992 and rapidly caused significant economic losses [2–4]. In Europe, the ALB was initially found in 2001 in Austria and has since been detected over almost all of Europe [5]. In the 1990s, the ALB was introduced to the Hexi Corridor region of northwestern China, leading to significant mortality in poplar shelterbelts [6]. The region's sparse precipitation and severe drought further weakened the trees, exacerbating the damage caused by the ALB. ALB adults were preferentially attracted to drought-stressed *A. negundo* trees [7]. Prompt monitoring of drought conditions is crucial for preventing ALB infestations. Although poplars under drought and ALB stress exhibit similar symptoms of water shortage, their causes and management differ. Drought is due to insufficient water, which will recover when irrigation is sufficient, but ALB damage is irrecoverable. As a borer pest, the ALB is mainly harmed by larvae tunneling in the cambial region and wood [8,9], disrupting

the tree's vascular tissues, hindering the upward transport of nutrients and water, and leading to tree death [10]. Timely detection and discrimination are essential for applying appropriate treatments based on the specific type of stress.

With continuous improvement in image resolution and data analytical methods, remote sensing has been widely applied to modern forestry management [11–13]. Hyperspectral imagery (HSI) contains spectral information in narrow bands, which provides insights into leaf pigmentation and physiological conditions, facilitating early detection of plant stress [14–16]. Light Detection and Ranging (LiDAR) data offer precise three-dimensional information, which enables gathering detailed information on the structural change of tree canopies under stress. Nonetheless, using either HSI or LiDAR data alone has limitations in assessment. For example, HSI cannot accurately discern the canopy structure and is highly susceptible to canopy shading, leading to reduced spectral information and altered shapes in the hyperspectral data [17]. LiDAR data can offer precise three-dimensional information to offset these limitations in HSI data [18]. A Support Vector Machine (SVM) is a widely used machine-learning algorithm known for its ability to handle complex decision boundaries and its effectiveness with small sample sizes while providing robust generalization performance [19]. To address the high dimensionality, collinearity, and risk of overfitting often associated with large datasets, Lv and Dai (2006) introduced the Partial Least Squares-Support Vector Machine (PLS-SVM) method. PLS-SVM uses PLS to extract key features from the data, reducing dimensionality and mitigating overfitting, and then uses these features as inputs for the SVM calibration model [20]. This approach not only enhances prediction precision but also significantly reduces modeling time compared to using SVM on the full dataset. In our study, we employed PLS-SVM to effectively reduce the dimensionality of both hyperspectral and LiDAR data, thereby preventing overfitting and enabling more efficient and accurate classification.

Some studies have focused on using hyperspectral images to discriminate the biotic and abiotic stress on plants [21–23]. Data dimensionality reduction and classification based on machine-learning methods were widely used [24]. Susič et al. (2018) used hyperspectral data and the PLS-SVM method to discriminate between nematode infestation and drought stress in tomato, which achieved up to 100% accuracy in differentiating between well-watered and water-deficient plants, and between 90 and 100% when identifying nematode-infested plants [21]. Ramamoorthy et al. (2022) used Principal component analysis and maximum likelihood classifiers to discriminate drought and root–knot nematode infestation in cotton and the results were promising [22]. Praprotnik et al. (2022) combined sparse partial least squares discriminant analysis and support vector machine classification of hyperspectral data to detect wireworm infestation and drought stress in Maize and obtained accuracies of 67–84.7% [23]. These experiments explored the discrimination between biotic and abiotic stresses but paid less attention to combined stress. Additionally, these studies relied solely on hyperspectral data and did not incorporate LiDAR to investigate 3D structural differences.

Generally, the Gobi Desert region of northwest China is in extreme drought, poplars require irrigation and are highly susceptible to ALB stress. Trees damaged by ALBs showed similar symptoms of water shortage as drought stress but significant differences in management. Timely detection of them is essential for applying appropriate treatments based on the specific type of stress. The goals of this study were to: (1) evaluate the capacity of UAV-hyperspectral and LiDAR data to detect and discriminate ALB damage, drought stress and combined stress; (2) explore how hyperspectral and LiDAR variables response to stresses and search for the most sensitive indices for detection.

2. Materials and Methods

2.1. Study Area

The research plots are located in Jiuquan City, Gansu Province, northwest China, which belong to the Gobi landform. The climate type is a continental arid climate. Average annual precipitation is 80 mm, but average annual evaporation reaches 2000 mm. In this

research, two forest farms with different water conditions (well irrigated and non-irrigated) and similarly aged trees were selected (Figure 1).
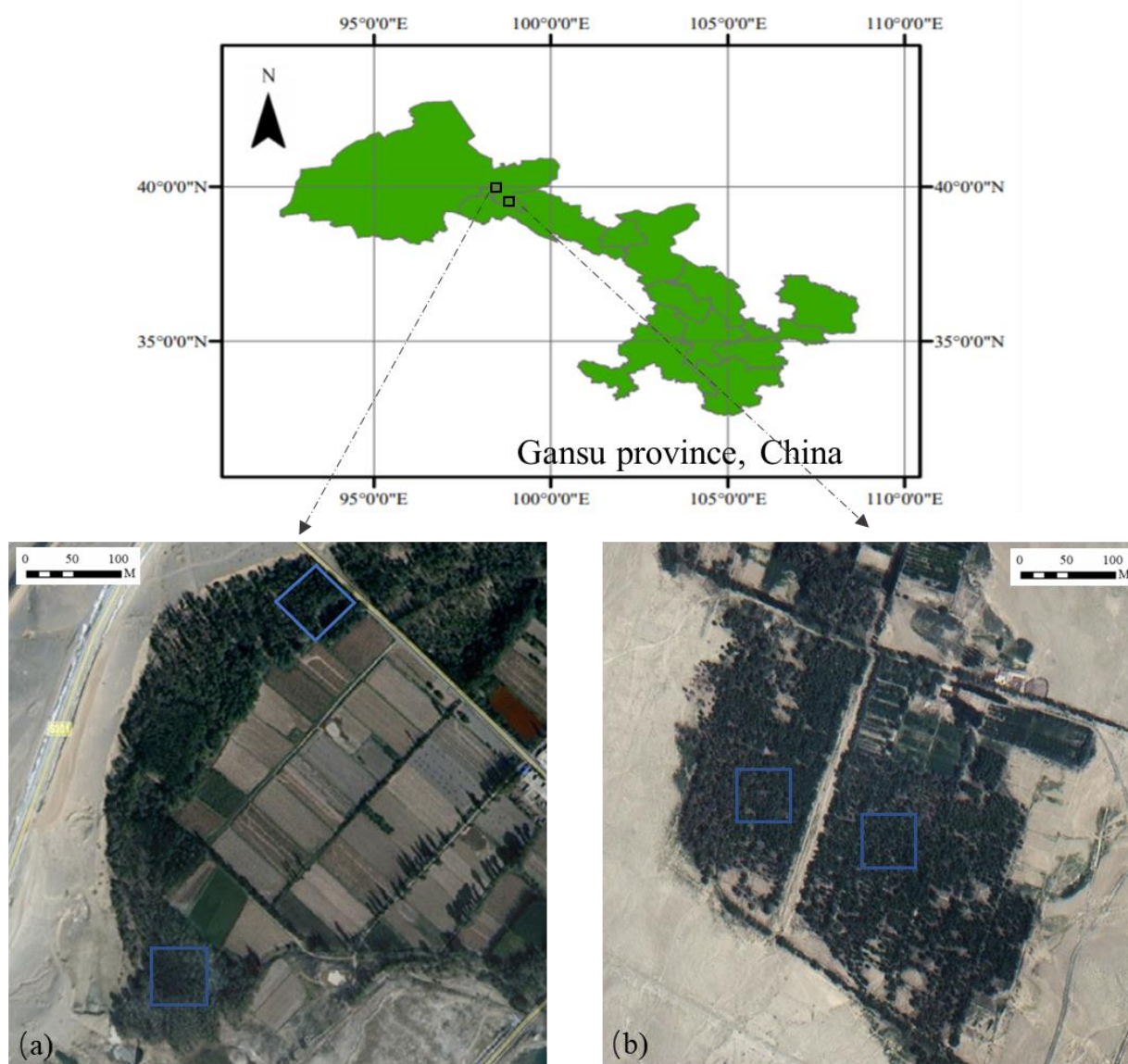

Figure 1. Study areas in this research. (**a**) Jiuquan Xincheng national Forest Farm (well watered). (**b**) Jiuquan Sanhe national Forest Farm (water deficient). Four sampled plots are marked blue.

Plot 1 (Figure 1a): Jiuquan Xincheng national Forest Farm (39°57′N, 98°23′E). Farmland windbreak forest, well irrigated, with surface water, including stands with health and ALB damage and a tree age of 40–60 years. The studied tree species were *Populus gansuensis*, *Populus alba* var. *pyramidalis*, and *Salix matsudana*.

Plot 2 (Figure 1b): Jiuquan Sanhe national Forest Farm (39°23′N, 99°04′E). Extremely poor irrigation conditions, no surface water, and there has been no normal irrigation for two years. The stand contains health and ALB damage, and the tree ages are 40–60 years. The studied tree species were the same as Plot 1.

Both farms contain poplars with health and ALB-damage. Both farms are located in a flat area at an elevation of 1480 m. Soil conditions are the same: brown desert soil with low organic matter content and poor nitrogen. Both plots are total covered with *Populus gansuensis*. We established two 50 × 50 m plots in each forest farms, for a total of four plots. There was a total of four types of sample trees: healthy (H), damaged only by ALBs (A),

damaged only by drought (D), and combined damaged by both ALBs and drought (AD) (Figure 2).
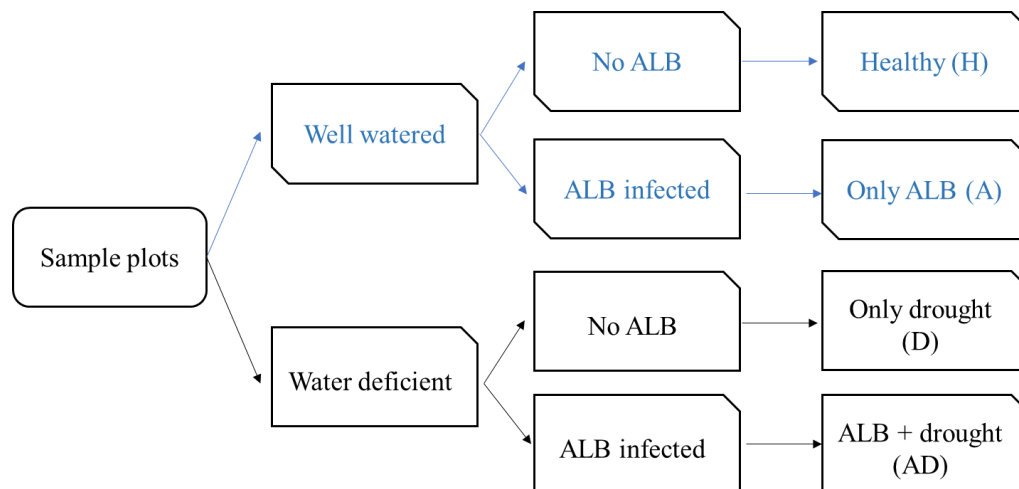

Figure 2. Four types of poplars in this experiment. Abbreviations of each sample of poplars are shown in brackets.

2.2. Determination of Soil Moisture Conditions

A FieldScout TDR-300 probe with 15 cm long TDR rods (Spectrum Technologies, Inc., Aurora, CO, USA) was used to measure the soil moisture content at each sample plot. Given the strong solar radiation over the Gobi Desert, we measured soil water content 50 cm below the surface to determine the drought status of each sample plot. The volumetric water content (VWC) was used to determine the degree of soil dryness, an indicator of drought [25]. Before measurement, we calibrated the meter to ensure the accuracy. We then randomly select ten points in each sample plot, taking the average value as the soil water content. Table 1 shows VWC of two forest farms.

Table 1. Volumetric water content (VWC) of two forest farms.

	Sanhe Forest Farm (Water Deficient)				Xincheng Forest Farm (Well Watered)			
	Mean	**Stdev**	**Max**	**Min**	**Mean**	**Stdev**	**Max**	**Min**
VWC (%)	17.82	3.73	25.2	11.8	61.1	7.44	67.7	49.2

t test *p* < 0.001.

2.3. Determination of ALB Damage and Measurement of Leaf Area Index

The Asian longhorned beetle is a hidden trunk borer. We determined whether the poplar is damaged by ALB by looking for funnel-shaped oviposition pit, defecation holes, and circular exit holes (Figure 3) [10]. If these symptoms appear on a poplar tree, we consider it to be damaged by ALBs. We also searched for crown thinning, which is easily identified and manifests itself as sparse leaves and dry branches. Leaf area index (LAI) represents leaf density and reflects biophysical abilities including photosynthesis and respiration [26]. We measured LAI to assess crown thinning by averaging four individual measurements taken in the cardinal directions of sample trees using the SmartLAI app [27]. A total of 325 poplars were surveyed: 66 healthy (H); 75 with only ALB stress (A); 80 with only drought stress (D); and 104 with both ALB and drought stress (AD). Table 2 shows the LAI of poplars under four types of stressors.
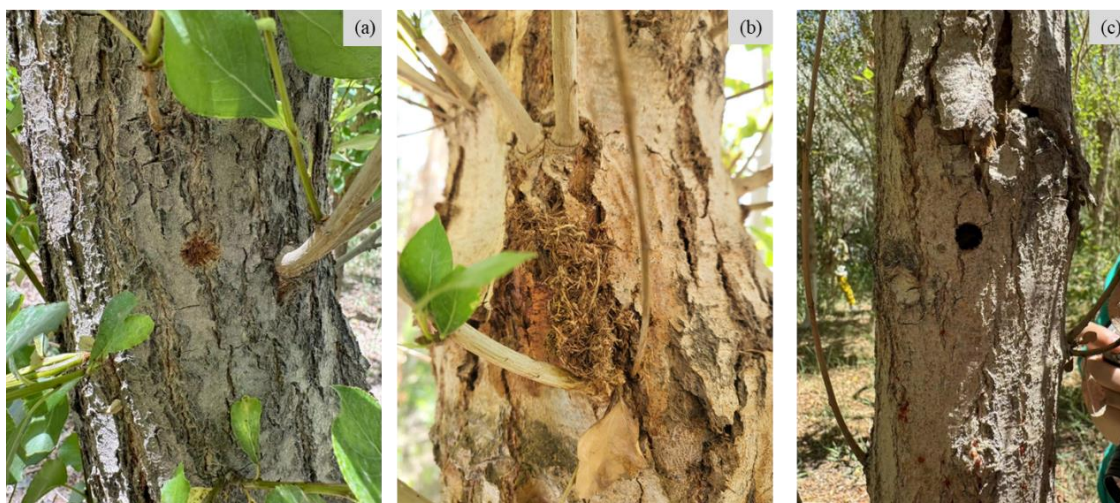
Figure 3. Evidence for determine ALB damage. (**a**) ALB adult grooving a funnel-shaped oviposition pit. (**b**) Frass discharged by ALB larvae. (**c**) Circular exit holes of ALB adults.

Table 2. Leaf area index of poplars stands under four types of stressors.

Stress Types	Leaf Area Index
Health	2.463 ± 0.399
ALB	2.052 ± 0.318
Drought	2.032 ± 0.280
ALB and drought	1.842 ± 0.221

2.4. UAV-Hyperspectral and LiDAR Data Acquisition and Pre-Processing

UAV-hyperspectral imagery (HSI) and LiDAR data were simultaneously collected using a DJI Matrice 600 UAV system (DJI, Shenzhen, China) during the same flight campaign (Figure 4). The mounting system enables the hyperspectral and LiDAR equipment to jointly use the UAV's Inertial Measurement Unit (IMU) and Global Positioning System (GPS), facilitating high-precision ortho-correction and data fusion. The UAV was also equipped with an RTK system for centimeter-precise positioning. Data were acquired for plot 1 (well watered) on 2 August 2021 from 12:20 to 12:50 PM and for plot 2 (water deficient) on 3 August 2021 from 11:50 AM to12:30 PM. Flights were conducted under a cloudless sky, at an altitude of 100 m, and a speed of 3 m/s, with imagery overlapping by 60% at the front and sides.

LiDAR data were collected with the LR1601-IRIS UAV-mounted system (IRIS Inc., Beijing, China). Its pulse repetition frequency was 5–20 Hz with two returns per pulse. Point density ranged from 100 to 900 points per m^2. The LiDAR data were preprocessed through strip alignment, noise point removal, and ground point classification using the LiDAR360 software (version 3.0, GreenValley International, Beijing, China). Digital Elevation Model (DEM) and Digital Surface Model (DSM) were generated with a spatial resolution of 0.1 m.

The HI sensor has a field of view of $10°$ and a focal length of 17 mm. The hyperspectral images encompassed 150 spectral bands, ranging from 400 to 1000 nm. Hyperspectral images were generated at a spatial resolution of 0.1 m. Reflectance correction and radiometric calibration were performed using a standard white board (Figure 4). Hyperspectral images were matched to LiDAR data with twelve ground control points (GCPs) with an overall root mean square errors (RMSEs) < 1 pixel.
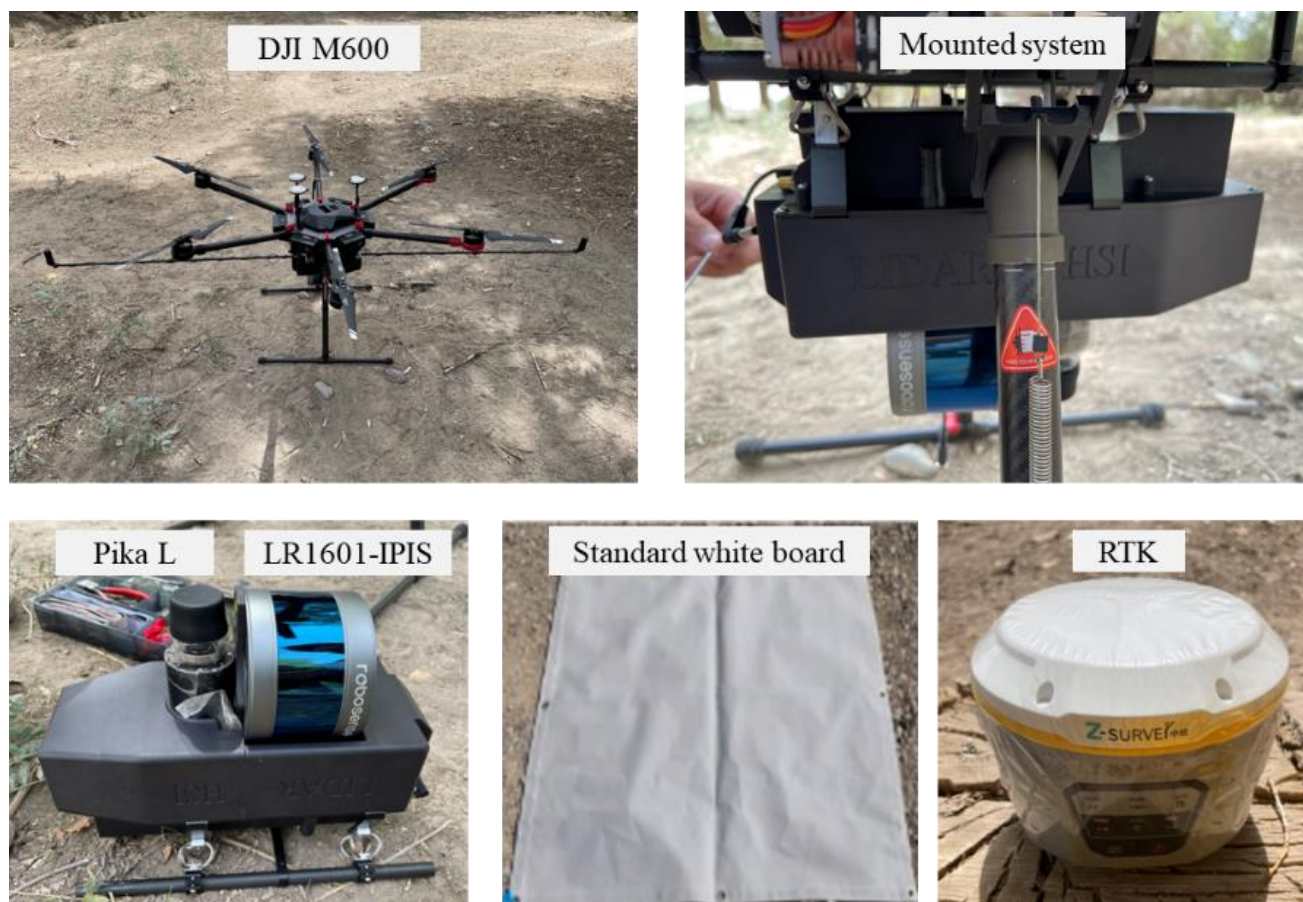
Figure 4. The UAV-mounted system in this research.

2.5. Extraction of Hyperspectral and LiDAR Features

A Canopy Height Model (CHM) segmentation algorithm in the LiDAR360 software (GreenValley Inc., Shanghai, China) was used to segment single trees [28]. The CHM, produced from DSM and DEM, also has a resolution of 0.1 m. Hyperspectral and LiDAR features for sample trees were extracted based on the CHM segmentation results. Sample trees incorrectly segmented by the CHM algorithm were manually delineated for extraction. Hyperspectral reflectance was computed only for sunlit pixels of each tree crowns. The hyperspectral reflectance of each canopy was smoothed using the second-order polynomial of the Savitzky–Golay filter. Table 3 summarizes the 23 spectral variables including twelve vegetation indices, five absorption bands, two red-edge parameters, and four absorption features. At the same time, 32 variables were extracted from the LiDAR including 14 variables related to the distribution of point-cloud heights, 13 metrics about the intensity of point-cloud, and five canopy densities based on all laser returns (Table 4) [29–31]. In total, 55 variables, comprising both hyperspectral and LiDAR features, were utilized for variable screening and developing the PLS-SVM classification model.

Table 3. Selection of candidate hyperspectral variables.

Variables Type	Variable	Formula and Description	Reference
Absorption bands	Spectral reflectance at λ nm ($R\lambda$)	λ = 430, 460, 640, 660, 970	[32]
Red edge parameters	Red-edge position linear interpolation (REP_LiA)	$700 + 40 \times ((R670 + R780)/2 - R700)/(R740 - R700)$	[33]
	dRE (AMP)	Max 1st derivative in red edge region	[34]

Table 3. *Cont.*

Variables Type	Variable	Formula and Description	Reference
Reflection and absorption features	Green peak reflectance (Rg)	Rmax (510, 560)	[35]
	Red valley reflectance (Rr)	Rmax (640, 680)	
	Green peak height (GH)	$1 - [R500 + 0.35\times (R670 - R500)]/R560$	
	Red valley depth (RD)	$1 - R670/[R560 + 0.55 \times (R760 - R560)]$	
Vegetation indexes (VIs)	Normalized difference vegetation index (NDVI)	$(R800 - R670)/(R800 + R670)$	[36]
	Green NDVI (GNDVI)	$(R800 - R550)/(R800 + R550)$	[37]
	Photochemical reflectance index (PRI)	$(R570 - R531)/(R531 + R570)$	[38]
	Plant senescing reflectance index (PSRI)	$(R680 - R500)/R750$	[39]
	Simple ratio index (SR)	$R800/R680$	[40]
	Vogelmann red edge index (VOG)	$(R734 - R747)/(R715 + R726)$	[41]
	Carter index (CI)	$R760/R695$	[42]
	Anthocyanin Reflectance Index (ARI)	$1/R550 - 1/R700$	[43]
	Carotenoids Index (CARI)	$(R720 - R521)/R521$	[44]
	Red-edge Chlorophyll Index (CIred-edge)	$(R750 + R705)/R705$	[45]
	Red Edge Normalized Difference Vegetation Index (RENDVI)	$(R750 - R705)/(R750 + R705)$	[46]
	Greenness Index (GI)	$R554/R677$	[47]

Table 4. Selection of candidate LiDAR metrics.

Variable Type	Formula or Variable Name	Definition
Distribution of point-cloud heights	Height_IQ/TH	Interquartile range of height percentile of crown return points (normalized by tree height)
	Height_P10/TH	10th height percentile of crown return points (normalized by tree height)
	Height_P25/TH	25th height percentile of crown return points (normalized by tree height)
	Height_P50/TH	50th height percentile of crown return points (normalized by tree height)
	Height_P75/TH	75th height percentile of crown return points (normalized by tree height)
	Height_P90/TH	90th height percentile of crown return points (normalized by tree height)
	Height_P99/TH	99th height percentile of crown return points (normalized by tree height)
	elev_aad	Average absolute deviation of elevations of all returns
	elev_IQ	Interquartile range of elevations of all returns
	elev_kurtosis	kurtosis of elevations of all returns
	elev_skewness	Skewness of elevations of all returns
	elev_sqrt_mean_sq	Quadratic mean of elevations of all returns
	elev_stddev	Standard deviation of elevations of all returns
	elev_variance	Variance of elevations of all returns

Table 4. *Cont.*

Variable Type	Formula or Variable Name	Definition
Density_metrics of all returns	density_metrics [1]	Densities of all returns in 10th interval
	density_metrics [3]	Densities of all returns in 30th interval
	density_metrics [5]	Densities of all returns in 50th interval
	density_metrics [7]	Densities of all returns in 70th interval
	density_metrics [9]	Densities of all returns in 90th interval
Intensity of point-cloud	int_percentile_25th	25th percentile of crown return intensity
	int_percentile_75th	75th percentile of crown return intensity
	int_percentile_90th	90th percentile of crown return intensity
	int_percentile_99th	99th percentile of crown return intensity
	int_aad	Average absolute deviation of intensities of all returns
	int_cv	Coefficient of variation of crown return intensity
	int_kurtosis	Kurtosis of intensities of all returns
	int_max	Maximum intensity of all returns
	int_mean	Mean intensity of all returns
	int_skewness	Skewness of intensities of all returns
	int_variance	Variance of intensities of all returns
	int_stddev	Standard deviation of intensities of all returns

2.6. PLS-SVM Model and Classification

Before modelling, we used partial least squares—variable importance in projection (VIP) for data mining and to reduce collinearity impact in variables, thus to simplify the model structure and improve classification accuracy [48]. The VIP values were calculated by each predictor's importance in reflecting the weighted sum of squares of the PLS weights, and its score estimates the importance of each variable in the projection used in the PLS model [49]. We selected the 10 variables with highest VIP values for each model to avoid overfitting in classification [50]. The capacity factor (C) and gamma values for the PLS-SVM classification were determined by performing a random search of several combinations of C and gamma [51]. The best combination of parameters was used to establish the PLS-SVM model. All variables were divided into a train-set and test-set in the ratio of 7 to 3. A 10-fold cross-validation method was used to assess model accuracy. The classification accuracy was evaluated using the producer's accuracy (PA), user's accuracy (UA), overall accuracy (OA), and the Kappa coefficient (K) derived from confusion matrices. These indicators provide a comprehensive assessment of the classification accuracy of the variables, with PA indicating the accuracy of each class, UA reflecting the reliability of the classified data, OA showing the overall correctness, and the Kappa coefficient accounting for chance agreement.

The hyperspectral and LiDAR parameters of 325 poplar trees were used for classifications according to the actual management needs (Figure 5).

- Model 1: Is the poplar under stress?
- Model 2: Is the poplar under drought?
- Model 3: Is the poplar under ALB stress?
- Model 4: Is the poplar healthy, under ALB stress, drought stress, or combined stress of drought and ALB?

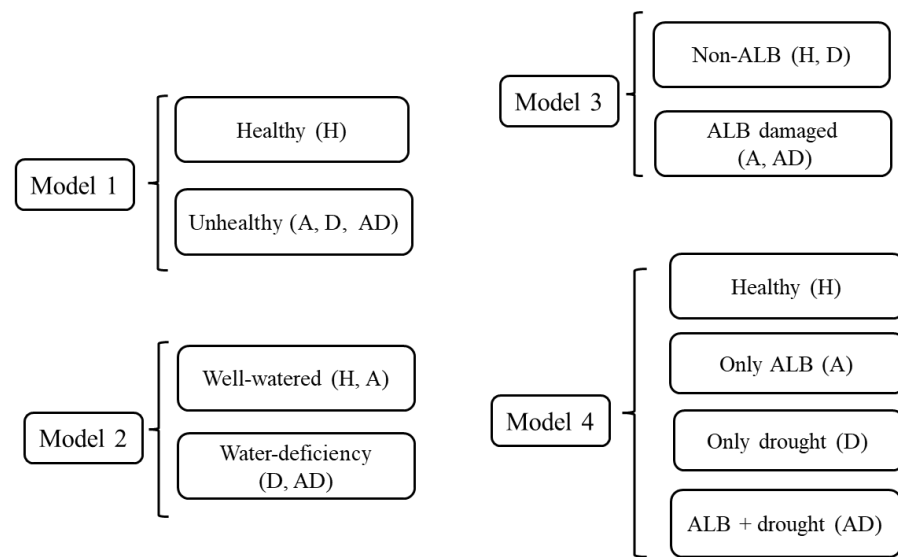The VIP analyses, PLS-SVM evaluation, and classification were performed using R software (version 4.1.2).

Figure 5. Four classification models according to the plantation management needs.

3. Results

3.1. Signatures of ALB and Drought Stress

The mean reflectance curves of poplars under different stresses within 400–1000 nm are shown in Figure 6. For different models, the differences of reflectance were most obvious in the green peak (500–600 nm) and NIR (750–1000 nm). Figure 7 illustrates ten typical hyperspectral indices and LiDAR metrics sensitive to stresses. Significant differences were observed in poplars under water-deficient conditions, particularly in elev_sqrt_mean_sq, which was notably lower in water-deficient poplars compared to those without water deficiency. Similarly, significant differences were found in poplars affected by ALB damage, especially in GH. The GH value in ALB-damaged poplars was significantly lower than in poplars without ALB damage.
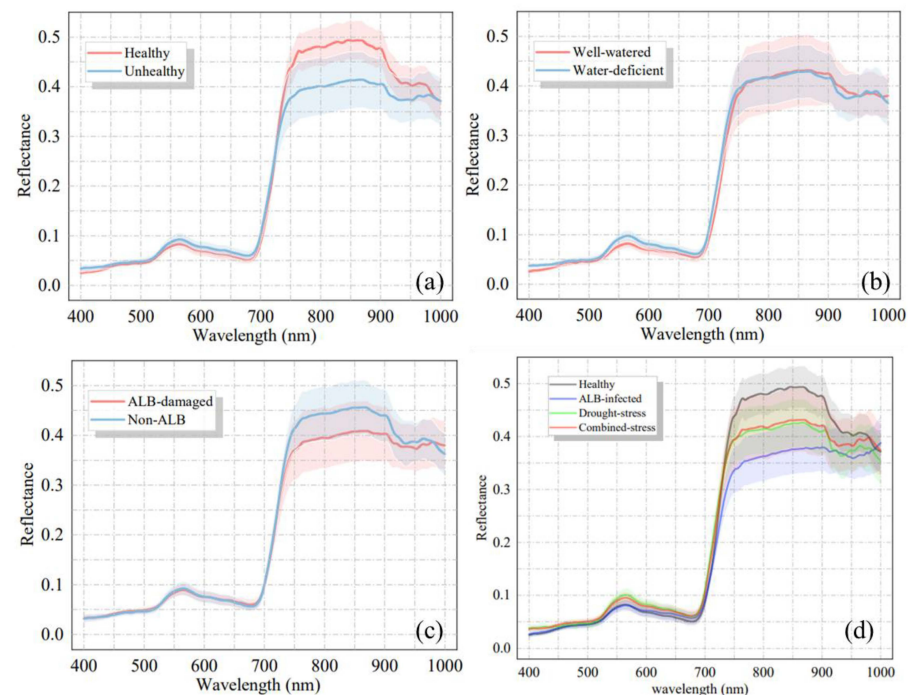

Figure 6. Mean spectral reflectance of poplars grouped according to: (**a**) Healthy/Unhealthy; (**b**) Well watered/Water deficient; (**c**) ALB damaged/Non-ALB; (**d**) Healthy/ALB infected/Drought stress/Combined stress. Note: The shaded region indicates the standard deviation of the mean value.
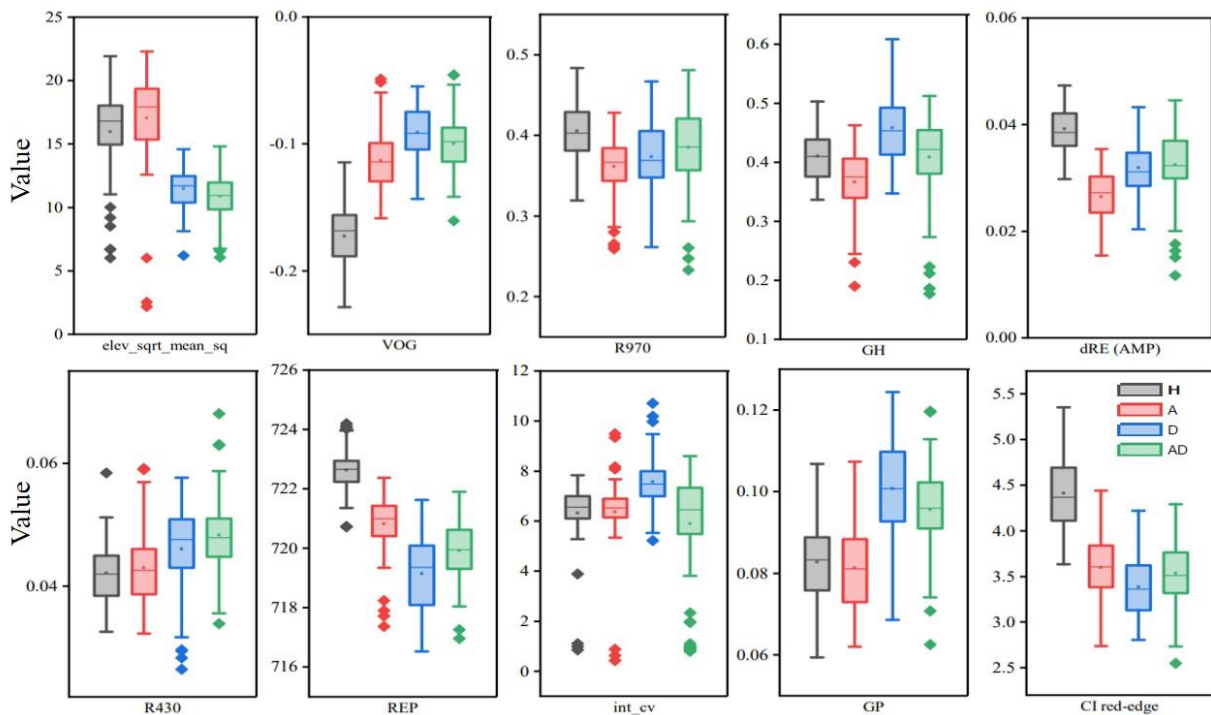
Figure 7. Ten typical parameters derived from hyperspectral and LiDAR images at different stress (H: Healthy; A: ALB stress; D: Drought stress; AD: ALB and Drought stress).

3.2. Classification Accuracy

The PLS-SVM classification results indicated it was possible to distinguish between biotic and abiotic stress on poplars, though detection accuracy varied significantly across different stress types (Figure 8). The accuracy for identifying healthy poplars was 94.79% (Model 1). The classification accuracy for drought-affected poplars was 94.85% (Model 2), while the accuracy for identifying ALB-damaged poplars was only 80.81% (Model 3). The overall classification accuracy for the four different stress types was 78.79% (Model 4).
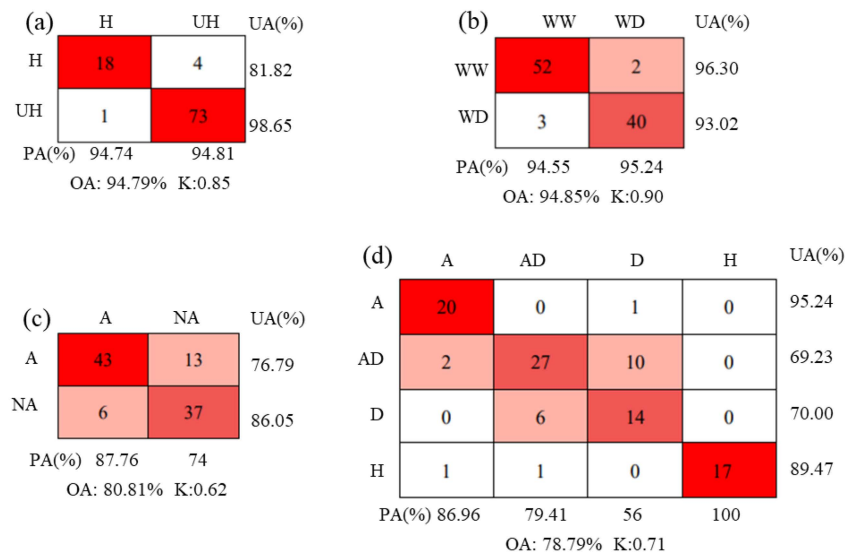

Figure 8. Confusion matrices for the five datasets based on PLS-SVM classification. (**a**) H: Healthy, UH: Unhealthy; (**b**) WW: Well watered, WD: Water deficiency (Drought); (**c**) A: ALB damaged, NA: Non-ALB; (**d**) H: Healthy, A: ALB stress, D: Drought stress, AD: ALB and Drought stress.

When classifying tree stress (or health—see below, model 1), the five most important parameters (VOG, REP, CIred-edge, RENDVI, CI) were related to the red edge in hyperspectral parameters and, thus, to leaf pigment. Compared with unhealthy poplar, healthy poplar showed lower value in VOG, and higher values in REP, CI red-edge, REND VI, and CI.

When classifying data based on whether trees were under drought stress (model 2), the five most obvious differences were elev_sqrt_mean_sq, REP, GP, VOG, and elev_stddev (Table 5). Among them, elev_sqrt_mean_SQ and elev_Stddev are related to the distribution of point cloud heights in LiDAR outputs. Compared with well-watered poplars, poplars under water deficiency showed lower values in elev_sqrt_mean_sq, REP, and elev_Stddev, and higher values in GP and VOG.

Table 5. Variables used in each PLS-SVM model. (Ranked from high to low according to VIP value, only the top ten most important classification variables are shown).

Model 1 (Healthy/Unhealthy)	Model 2 (Well-Watered/ Water-Deficient)	Model 3 (ALB-Damaged/ Non-ALB)	Model 4 (Health/Only ALB-Infected/Only Water-Deficient/Combined Damages)
VOG	elev_sqrt_mean_sq	R970	elev_sqrt_mean_sq
REP	REP	Height_P99/TH	VOG
CI red-edge	GP	int_cv	R970
RENDVI	VOG	VOG	GH
CI	elev_stddev	dRE (AMP)	dRE (AMP)
dRE (AMP)	R430	GH	R430
SR	elev_variance	Height_P90/TH	REP
GNDVI	CI red-edge	PSRI	int_cv
R970	RENDVI	R430	GP
elev_stddev	GH	GP	CI red-edge

When classifying whether the trees were under biotic ALB stress (model 3), the most obvious differences appeared in R970, Height_99th/Tree Height, int_cv, VOG, and dRE (AMP) (Table 5). The R970 is a hyperspectral near-infrared band and related to plant water and chlorophyll content [32]. The variable Height_99th/Tree Height was the 99th percentile height of crown return points (normalized by tree height) from LiDAR. This was closely related to the dry treetop characteristics of poplar that ALB damaged. The int_cv is a radar intensity variable, indicating the coefficient of variation of crown return intensity. Compared with non-ALB poplars, poplars under ALB-damage showed lower values in R970, Height_99th/Tree Height, int_cv, and higher values in VOG and dRE (AMP).

When classifying whether trees were healthy, only under ALB stress, only under drought stress, or under the combined stress of drought and ALB (model 4), the most obvious differences lie in elev_sqrt_mean_sq, VOG, R970, GH, and dRE (AMP). Detection of ALBs in poplars improved when the stand was well watered. The Producer's accuracy of well-watered poplars under ALB damage was 86.96%. However, the Producer's accuracy of poplars with insufficient water under ALB damage was only 79.41% (Figure 8d).

4. Discussion

4.1. Optimal Variables for Classification

The research evaluated 23 hyperspectral vegetation indices and 32 LiDAR metrics using PLS-VIP to assess their responsiveness to drought and ALB stress. The LiDAR metric (elev_sqrt_mean_sq) proved crucial for drought detection, whereas the hyperspectral band (R970) was key in identifying ALB, underscoring the need to integrate both sensors. The elev_sqrt_mean_sq represents the quadratic mean of elevations of all returns in LiDAR data, typically used to indicate the surface complexity of forest or vegetative cover. A higher quadratic mean may indicate greater canopy height and density, and a more complex vegetation structure [52–54]. In poplars subjected to drought stress, leaf sparsity and

a lower leaf area index compared to healthy poplars were observed, leading to a low elev_sqrt_mean_sq values (Table 2). R970 is in the near-infrared region, which is sensitive to vegetation water and chlorophyll content, as well as overall plant health. Healthy vegetation exhibits higher reflectance at R970, while stressed vegetation, due to reduced water and chlorophyll content, shows lower reflectance [55,56]. ALB damage impedes the transport of water and nutrients in trees, leading to insufficient water in the leaves and degradation of chlorophyll [57,58].

Previous studies on monitoring forest stress using UAV-hyperspectral and LiDAR mainly focuses on detecting pests and diseases in coniferous trees, in which LiDAR was just a tool for single tree segmentation and providing structure information for hyperspectral image. LiDAR alone cannot effectively detect forest pest for it cannot reveal the biochemical condition of trees [17,18]. Unlike previous studies, in this experiment, LiDAR metrics effectively detect forest pest. The primary reason for this may be that as a broadleaf tree, the three-dimensional structure of poplar canopies is highly sensitive and responsive to stress [59]. Poplars under drought and ALB stress displayed dried-up leaves when compared with healthy poplars. But the location of dried-up leaves could only be detected using vertical canopy features of LiDAR data, which confirms the utility of LiDAR's three-dimensional structural analysis in monitoring ALB and drought stress in poplar trees.

4.2. Discrimination Performance for Biotic and Abiotic Stress

By combining UAV-hyperspectral and LiDAR data with PLS-SVM, we successfully detected and differentiated biotic and abiotic stresses in poplars. The accuracy reached 94.85% accuracy in detecting drought and 80.81% accuracy for ALB damage. The overall classification accuracy stood at 78.79% for four poplar categories: healthy, ALB-affected only, drought-affected only, and those with combined drought and ALB damage. Poplar trees under drought were detected more accurately (OA: 94.85%, K: 0.90). However, the accuracy for detecting ALB-induced damage in poplars was notably lower (OA: 80.81%, K: 0.62). This indicates that the phenotypic changes caused by ALB are more subtle compared to those induced by drought, making them more difficult to detect. ALB damage detection was more reliable in well-irrigated conditions (PA: 86.96%) compared to water-deficient conditions (PA: 79.41%) (Figure 8d). This indicated that drought-induced effects can mask the specific spectral and structural changes indicative of ALB damage. Global warming is predicted to lead to more severe droughts in forest ecosystems, resulting in more severe biotic stress. Many tree-boring pests act as secondary invaders. For example, *Ips typographus* Linnaeus preferentially attacks weak trees [60,61]. ALB adults showed a preference for drought-stressed *A. negundo* trees [7]. Drought-induced weakening is likely to worsen the impact of tree-boring beetles. Prompt monitoring of drought is crucial for ALB prevention. Remote sensing applications in forestry offer solutions to these challenges in modern forest management.

This study was conducted in August but lacked a time-series analysis to determine a time-stable indicators for detecting poplars under pest and drought stress across their phenological stages, highlighting a key area for future research. The impact of phenology on broadleaf trees is unavoidable. Broadleaf tree leaves naturally wither at the end of the growing season, even in the absence of stress. The stresses may cause the trees to wither earlier than phenology, which needs further investigation. Additionally, the life cycle of the pest may also affect the detection of borer pests. ALB undergoes various stages in its life cycle, such as prepupae, pupae, adults, eggs, and larvae, with the larval stage was considered as the main damage period [62]. The best option is to find a time-stable indicator for accurately detecting ALB before the adults lay new eggs during the growing seasons, which needs a time-series study within the growing seasons.

4.3. Selecting Variables Based on ALB Damage Characteristics

Distinguishing between various stresses necessitates stress-specific parameters (Table 5). Unique symptoms exhibited by trees under specific stress should be consid-

ered [63,64]. Although ALB-induced damage resembles drought-related tree death, they manifest differently in trees. Drought, as a systemic stressor, induces widespread leaf senescence throughout trees [65,66], whereas ALB damage initiates senescence at the canopy's top (Figure 9). This treetop dieback is determined by the biological behavior of the ALB. The main damage period occurs during the larval stage, wherein the larvae consume the phloem, disrupting the upward transport of water and nutrients in the trees [2,9,67]. Additionally, female ALBs prefer laying eggs in the upper trunk regions, concentrating the larvae in the tree's upper parts [68]. In this research, Height_99th/Tree Height from the LiDAR metric was correlates strongly correlates with ALB-damaged poplars for it ranks as the second most significant variable for ALB detection (Table 5). It represents the ratio of the 99th percentile height of all returns to the average tree height and was commonly used to monitor canopy loss and reductions in aboveground biomass in stressed forests [69,70]. Selecting variables based on ALB damage characteristics can notably decrease the workload involved in variable selection. However, this approach may have two limitations: first, it requires a higher point cloud density of LiDAR; second, the differences may not be evident at early stage of damage. Early stress detection necessitates further exploration of spectral data within the narrow bands of the hyperspectral spectrum [17,71,72].
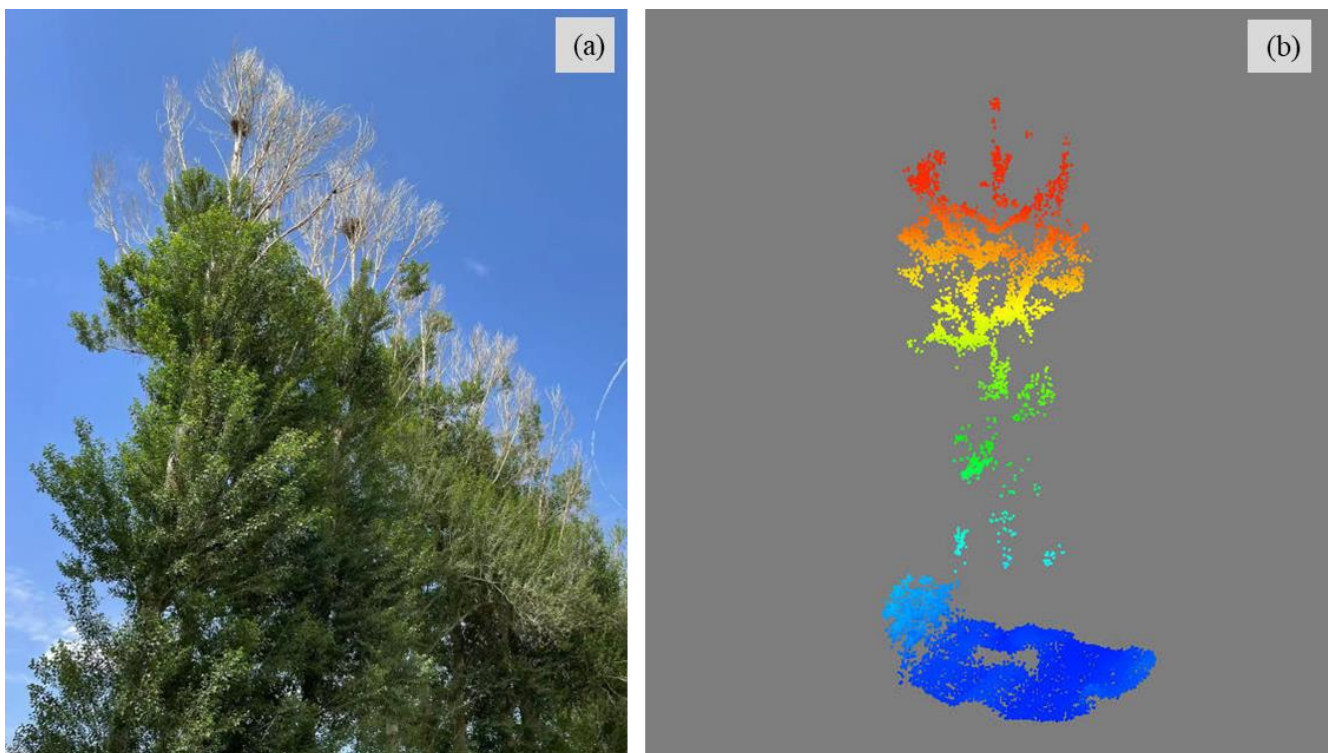

Figure 9. Dried tops of poplars under ALB damage. (**a**) RGB image. (**b**) LiDAR image.

5. Conclusions

Our research demonstrated the combination of a UAV-hyperspectral image and LiDAR could detect and discriminate ALB and drought stress in poplar trees. The PLS-SVM classification achieved 94.85% accuracy in distinguishing between well-watered and water-deficient trees, and 80.81% accuracy in detecting ALB damage. The overall classification accuracy stood at 78.79% for classifying four poplar categories: healthy, ALB-affected only, drought-affected only, and those with combined drought and ALB damage. The developed classification models provide a valuable tool for detecting and differentiating stress types, enabling timely interventions such as irrigation or pest control in poplar forests, particularly in the challenging conditions of the Gobi Desert.

References

1. Pedlar, J.H.; McKenney, D.W.; Yemshanov, D.; Hope, E.S. Potential Economic Impacts of the Asian Longhorned Beetle (Coleoptera: Cerambycidae) in Eastern Canada. *J. Econ. Entomol.* **2020**, *113*, 839–850. [CrossRef] [PubMed]
2. Haack, R.A.; Law, K.R.; Mastro, V.C.; Ossenbruggen, H.S.; Raimo, B.J. New York's battle with the Asian long-horned beetle. *J. For.* **1997**, *95*, 11–15. [CrossRef]
3. Colautti, R.I.; Bailey, S.A.; VanOverdijk, C.D.; Amundsen, K.; MacIsaac, H.J. Characterised and projected costs of nonindigenous species in Canada. *Biol. Invasions* **2006**, *8*, 45–59. [CrossRef]
4. Nowak, D.J.; Pasek, J.E.; Sequeira, R.A.; Crane, D.E.; Mastro, V.C. Potential effect of Anoplophora glabripennis (Coleoptera: Cerambycidae) on urban trees in the United States. *J. Econ. Entomol.* **2001**, *94*, 116–122. [CrossRef]
5. Javal, M.; Roques, A.; Haran, J.; Hérard, F.; Keena, M.; Roux, G. Complex invasion history of the Asian longhorned beetle: Fifteen years after first detection in Europe. *J. Pest Sci.* **2017**, *92*, 173–187. [CrossRef]
6. Hu, J.; Angeli, S.; Schuetz, S.; Luo, Y.; Hajek, A.E. Ecology and management of exotic and endemic Asian longhorned beetle Anoplophora glabripennis. *Agric. For. Entomol.* **2009**, *11*, 359–375. [CrossRef]
7. Jin, Y.J.; Li, J.Q.; Li, J.G.; Luo, Y.Q.; Teale, S.A. Olfactory response of Anoplophora glabripennis to volatile compounds from ash-leaf maple (*Acer negundo*) under drought stress. *Sci. Silvae Sin.* **2004**, *40*, 99–105. (In Chinese)
8. Adachi, I. Development and life cycle of *Anoplophora malasiaca* (Thomson) (Coleoptera: Cerambycidae) on citrus trees under fluctuating and constant temperature regimes. *Appl. Entomol. Zool.* **1994**, *29*, 485–497. [CrossRef]
9. Qin, X.X.; Gao, R.T.; Li, J.Z.; Hao, W.Q.; Liu, K.J. A preliminary investigation on the resistance of different clones of poplar to *Anoplophora glabripennis* (Motsch.). *Sci. Silvae Sin.* **1985**, *21*, 310–314.
10. Haack, R.A.; Hérard, F.; Sun, J.; Turgeon, J.J. Managing invasive populations of Asian longhorned beetle and citrus longhorned beetle: A worldwide perspective. *Annu. Rev. Entomol.* **2010**, *55*, 521–546. [CrossRef]
11. Zhao, X.W.; Li, C.G.; Si, L.; Yuan, K.X.; Tian, Y.L. Building a new system of forest resources inventory by information technology. *J. Beijing For. Univ.* **2002**, *24*, 147–155.
12. Gleason, C.J.; Im, J. A Review of Remote Sensing of Forest Biomass and Biofuel: Options for Small-Area Applications. *GIScience Remote Sens.* **2011**, *48*, 141–170. [CrossRef]
13. Lippitt, C.D.; Stow, D.A.; Riggan, P.J. Application of the remote-sensing communication model to a time-sensitive wildfire remote-sensing system. *Int. J. Remote Sens.* **2016**, *37*, 3272–3292. [CrossRef]
14. Hernández-Clemente, R.; Hornero, A.; Mottus, M.; Penuelas, J.; González-Dugo, V.; Jiménez, J.C.; Suárez, L.; Alonso, L.; Zarco-Tejada, P.J. Early Diagnosis of Vegetation Health from High-Resolution Hyperspectral and Thermal Imagery: Lessons Learned From Empirical Relationships and Radiative Transfer Modelling. *Curr. For. Rep.* **2019**, *5*, 169–183. [CrossRef]
15. Nicotra, A.B.; Hofmann, M.; Siebke, K.; Ball, M.C. Spatial patterning of pigmentation in evergreen leaves in response to freezing stress. *Plant Cell Environ.* **2003**, *26*, 1893–1904. [CrossRef]
16. Bell, T.W.; Cavanaugh, K.C.; Siegel, D.A. Remote monitoring of giant kelp biomass and physiological condition: An evaluation of the potential for the Hyperspectral Infrared Imager (HyspIRI) mission. *Remote Sens. Environ.* **2015**, *167*, 218–228. [CrossRef]
17. Lin, Q.; Huang, H.; Wang, J.; Huang, K.; Liu, Y. Detection of Pine Shoot Beetle (PSB) Stress on Pine Forests at Individual Tree Level using UAV-Based Hyperspectral Imagery and LiDAR. *Remote Sens.* **2019**, *11*, 2540. [CrossRef]
18. Yu, R.; Luo, Y.; Zhou, Q.; Zhang, X.; Ren, L. A machine learning algorithm to detect pine wilt disease using UAV-based hyperspectral imagery and LiDAR data at the tree level. *Int. J. Appl. Earth Obs. Geoinf.* **2021**, *101*, 102363. [CrossRef]
19. Sánchez, A.V.D. Advanced support vector machines and kernel methods. *Neurocomputing* **2003**, *55*, 5–20. [CrossRef]
20. Lv, J.; Dai, L. Application of partial least squares support vector machines (PLS-SVM) in spectroscopy quantitative analysis. In Proceedings of the 6th World Congress on Intelligent Control and Automation, Dalian, China, 21–23 June 2006; Institute of Electrical and Electronics Engineers Inc.: Piscataway, NJ, USA, 2006; pp. 5228–5232. [CrossRef]
21. Susič, N.; Žibrat, U.; Širca, S.; Strajnar, P.; Razinger, J.; Knapič, M.; Vončina, A.; Urek, G.; Stare, B.G. Discrimination between abiotic and biotic drought stress in tomatoes using hyperspectral imaging. *Sens. Actuators B Chem.* **2018**, *273*, 842–852. [CrossRef]
22. Ramamoorthy, P.; Samiappan, S.; Wubben, M.J.; Brooks, J.P.; Shrestha, A.; Panda, R.M.; Reddy, K.R.; Bheemanahalli, R. Hyperspectral Reflectance and Machine Learning Approaches for the Detection of Drought and Root–Knot Nematode Infestation in Cotton. *Remote Sens.* **2022**, *14*, 4021. [CrossRef]

23. Praprotnik, E.; Vončina, A.; Žigon, P.; Knapič, M.; Susič, N.; Širca, S.; Vodnik, D.; Lenarčič, D.; Lapajne, J.; Žibrat, U.; et al. Early Detection of Wireworm (Coleoptera: Elateridae) Infestation and Drought Stress in Maize Using Hyperspectral Imaging. *Agronomy* **2023**, *13*, 178. [CrossRef]

24. Pantazi, X.E.; Moshou, D.; Oberti, R.; West, J.; Mouazen, A.M.; Bochtis, D. Detection of biotic and abiotic stresses in crops by using hierarchical self-organizing classifiers. *Precis. Agric.* **2017**, *18*, 383–393. [CrossRef]

25. Flax, N.J.; Currey, C.J.; Litvin, A.G.; Schrader, J.A.; Grewell, D.; Graves, W.R. Aesthetic Quality and Strength of Bioplastic Biocontainers at Different Substrate Volumetric Water Contents. *HortScience* **2018**, *53*, 483–490. [CrossRef]

26. Liu, Y.; Liu, R.; Chen, J.; Cheng, X.; Zheng, G. Current status and perspectives of leaf area index retrieval from optical remote sensing data. *Geo-Inf. Sci.* **2013**, *15*, 734–743. (In Chinese) [CrossRef]

27. Qu, Y.; Meng, J.; Wan, H.; Li, Y. Preliminary study on integrated wireless smart terminals for leaf area index measurement. *Comput. Electron. Agric.* **2016**, *129*, 56–65. [CrossRef]

28. Chen, Q.; Baldocchi, D.; Gong, P.; Kelly, M. Isolating Individual Trees in a Savanna Woodland Using Small Footprint LiDAR Data. *Remote Sens. Environ.* **2006**, *72*, 923–932. [CrossRef]

29. Lim, K.; Hopkinson, C.; Treitz, P. Examining the effects of sampling point densities on laser canopy height and density metrics. *For. Chron.* **2008**, *84*, 876–885. [CrossRef]

30. Liu, L.; Coops, N.C.; Aven, N.W.; Pang, Y. Mapping urban tree species using integrated airborne hyperspectral and LiDAR remote sensing data. *Remote Sens. Environ.* **2017**, *200*, 170–182. [CrossRef]

31. Zlonis, E.J.; Deo, R.; Berdeen, J.B. LiDAR and multispectral imagery predict the occurrence of tree cavities suitable for a cavity-nesting duck. *Remote Sens. Ecol. Conserv.* **2021**, *8*, 191–207. [CrossRef]

32. Curran, P.J. Remote sensing of foliar chemistry. *Remote Sens. Environ.* **1989**, *30*, 271–278. [CrossRef]

33. Guyot, G.; Baret, F. Utilisation de la haute resolution spectrale pour suivre l'etat des couverts vegetaux. In Proceedings of the Fourth International Colloquium on Spectral Signatures of Objects in Remote Sensing, ESA, SP-287, Assois, France, 18–22 January 1998; Guyenne, T.D., Hunt, J.J., Eds.; pp. 279–286.

34. Horler, D.N.H.; Dockray, M.; Barber, J. The red-edge of plant leaf reflectance. *Int. J. Remote Sens.* **1983**, *4*, 273–288. [CrossRef]

35. Wang, H.; Shi, L.; Ma, Y.; Shu, Q.; Liao, J.; Du, T. Research of Damage Monitoring Models and Judgment Rules of Pinus yunnanensis with Tomicus yunnanensis. *For. Res.* **2018**, *31*, 53–60.

36. Tucker, C.J. Red and photographic infrared linear combinations for monitoring vegetation. *Remote Sens. Environ.* **1979**, *8*, 127–150. [CrossRef]

37. Gitelson, A.A.; Kaufman, Y.J.; Merzlyak, M.N. Use of a green channel in remote sensing of global vegetation from EOS-MODIS. *Remote Sens. Environ.* **1996**, *58*, 289–298. [CrossRef]

38. Gamon, J.A.; Peñuelas, J.; Field, C.B. A Narrow-waveband spectral index that tracks diurnal changes in photosynthetic efficiency. *Remote Sens. Environ.* **1992**, *41*, 35–44. [CrossRef]

39. Merzlyak, M.N.; Gitelson, A.A.; Chivkunova, O.B.; Rakitin, V.Y. Non-destructive optical detection of pigment changes during leaf senescence and fruit ripening. *Physiol. Plant.* **1999**, *106*, 135–141. [CrossRef]

40. Jordan, C.F. Derivation of leaf area index from quality of light on the forest floor. *Ecology* **1969**, *50*, 663–666. [CrossRef]

41. Vogelman, J.E.; Rock, B.N.; Moss, D.M. Red-edge spectral measurements from sugar maple leaves. *Int. J. Remote Sens.* **1993**, *14*, 1563–1575. [CrossRef]

42. Carter, G.A. Ratios of leaf reflectance in narrow wavebands as indicator of plant stress. *Int. J. Remote Sens.* **1994**, *15*, 697–704. [CrossRef]

43. Gitelson, A.A.; Merzlyak, M.N.; Chivkunova, O.B. Optical properties and nondestructive estimation of anthocyanin content in plant leaves. *Photochem. Photobiol.* **2001**, *74*, 38–45. [CrossRef] [PubMed]

44. Zhou, X.; Huang, W.; Kong, W.; Ye, H.; Dong, Y.; Casa, R. Assessment of leaf carotenoids content with a new carotenoid index: Development and validation on experimental and model data. *Int. J. Appl. Earth Obs. Geoinf.* **2017**, *57*, 24–35. [CrossRef]

45. Gitelson, A.A.; Viña, A.; Ciganda, V.; Rundquist, D.C.; Arkebauer, T.J. Remote estimation of canopy chlorophyll content in crops. *Res. Lett.* **2005**, *32*, L08403. [CrossRef]

46. Gitelson, A.; Merzlyak, M.N. Spectral reflectance changes associated with autumn senescence of Aesculus hippocastanum L. and Acer platanoides L. leaves. Spectral features and relation to chlorophyll estimation. *J. Plant Physiol.* **1994**, *143*, 286–292. [CrossRef]

47. Smith, R.; Adams, J.; Stephens, D.; Hick, P. Forecasting wheat yield in a Mediterranean-type environment from the NOAA satellite. *Aust. J. Agric. Res.* **1995**, *46*, 113–125. [CrossRef]

48. Jamali-Dolatabad, M.; Sadeghi-Bazargani, H.; Sarbakhsh, P. Predictors of fatal outcomes in pedestrian accidents in Tabriz Metropolis of Iran: Application of PLS-DA method. *Traffic Inj. Prev.* **2019**, *20*, 873–879. [CrossRef]

49. Wang, Z.X.; He, Q.P.; Wang, J. Comparison of variable selection methods for PLS-based soft sensor modeling. *J. Process. Control.* **2015**, *26*, 56–72. [CrossRef]

50. Chong, I.-G.; Jun, C.-H. Performance of some variable selection methods when multicollinearity is present. *Chemom. Intell. Lab. Syst.* **2005**, *78*, 103–112. [CrossRef]

51. Bergstra, J.; Bengio, Y. Random search for hyper-parameter optimization. *J. Mach. Learn. Res.* **2012**, *13*, 281–305.

52. Peter, J.S.; Drake, J.; Medley, P.; Ibeanusi, V. Forest Structural Estimates Derived Using a Practical, Open-Source LiDAR-Processing Workflow. *Remote Sens.* **2021**, *13*, 4763. [CrossRef]

53. Pirotti, F. AAnalysis of Full-Waveform LiDAR Data for Forestry Applications: A Review of Investigations and Methods. *iForest-Biogeosciences For.* **2011**, *4*, 100–106. [CrossRef]

54. Akay, A.E.; Oğuz, H.; Karas, I.R.; Aruga, K. Using LiDAR Technology in Forestry Activities. *Environ. Monit. Assess.* **2009**, *151*, 117–125. [CrossRef] [PubMed]

55. Duarte, A.; Borralho, N.; Cabral, P.; Caetano, M. Recent Advances in Forest Insect Pests and Diseases Monitoring Using UAV-Based Data: A Systematic Review. *Forests* **2022**, *13*, 911. [CrossRef]

56. Yu, R.; Ren, L.L.; Luo, Y.Q. Early detection of pine wilt disease in Pinus tabuliformis in North China using a field portable spectrometer and UAV-based hyperspectral imagery. *For. Ecosyst.* **2021**, *8*, 44. [CrossRef]

57. Shi, Y.; Skidmore, A.K.; Wang, T.; Holzwarth, S.; Heiden, U.; Pinnel, N.; Zhu, X.; Heurich, M. Tree species classification using plant functional traits from LiDAR and hyperspectral data. *Int. J. Appl. Earth Obs. Geoinf.* **2018**, *73*, 207–219. [CrossRef]

58. Goetz, A.F.H.; Vane, G.; Solomon, J.E.; Rock, B.N. Imaging spectrometry for earth remote sensing. *Science* **1985**, *228*, 1147–1153. [CrossRef]

59. Monclus, R.; Dreyer, E.; Villar, M.; Delmotte, F.M.; Delay, D.; Petit, J.; Barbaroux, C.; Le Thiec, D.; Bréchet, C.; Brignolas, F. Impact of drought on productivity and water use efficiency in 29 genotypes of Populus deltoides× Populus nigra. *New Phytol.* **2005**, *169*, 765–777. [CrossRef] [PubMed]

60. Holuša, J.; Hlásny, T.; Modlinger, R.; Lukášová, K.; Kula, E. Felled trap trees as the traditional method for bark beetle control: Can the trapping performance be increased? *For. Ecol. Manag.* **2017**, *404*, 165–173. [CrossRef]

61. Liu, Y.; Zhan, Z.; Ren, L.; Ze, S.; Yu, L.; Jiang, Q.; Luo, Y. Hyperspectral evidence of early-stage pine shoot beetle attack in Yunnan pine. *For. Ecol. Manag.* **2021**, *497*, 119505. [CrossRef]

62. Wang, L.; Li, C.; Luo, Y.; Wang, G.; Dou, Z.; Haq, I.U.; Shang, S.; Cui, M. Current and future control of the wood-boring pest *Anoplophora glabripennis*. *Insect Sci.* **2023**, *30*, 1534–1551. [CrossRef]

63. Li, Y.; Su, Y.; Hu, T.; Xu, G.; Guo, Q. Retrieving 2-D leaf angle distributions for deciduous trees from terrestrial laser scanner data. *IEEE Trans. Geosci. Remote Sens.* **2018**, *56*, 4945–4955. [CrossRef]

64. Junttila, S.; Holopainen, M.; Vastaranta, M.; Lyytikäinen-Saarenmaa, P.; Kaartinen, H.; Hyyppä, J.; Hyyppä, H. The potential of dual-wavelength terrestrial lidar in early detection of *Ips typographus* (L.) infestation—Leaf water content as a proxy. *Remote Sens. Environ.* **2019**, *231*, 111–264. [CrossRef]

65. Leuzinger, S.; Zotz, G.; Asshoff, R.; Körner, C. Responses of deciduous forest trees to severe drought in Central Europe. *Tree Physiol.* **2005**, *25*, 641–650. [CrossRef] [PubMed]

66. Tan, S.; Sha, Y.; Sun, L.; Li, Z. Abiotic Stress-Induced Leaf Senescence: Regulatory Mechanisms and Application. *Int. J. Mol. Sci.* **2023**, *24*, 11996. [CrossRef]

67. Gao, R.; Qin, X.; Chen, D.; Chen, W. A study on the damage to poplar caused by Anoplophora glabripennis. *For. Res.* **1993**, *6*, 189–193.

68. Haack, R.A. Exotic bark- and wood-boring Coleoptera in the United States: Recent establishments and interceptions. *Can. J. For. Res.* **2006**, *36*, 269–288. [CrossRef]

69. Silva, V.S.d.; Silva, C.A.; Mohan, M.; Cardil, A.; Rex, F.E.; Loureiro, G.H.; Almeida, D.R.A.d.; Broadbent, E.N.; Gorgens, E.B.; Dalla Corte, A.P.; et al. Combined impact of sample size and modeling approaches for predicting stem volume in *Eucalyptus* spp. forest plantations using field and LiDAR data. *Remote Sens.* **2020**, *12*, 1438. [CrossRef]

70. Goodwin, N.R.; Coops, N.C.; Culvenor, D.S. Assessment of forest structure with airborne LiDAR and the effects of environmental stressors. *Remote Sens. Environ.* **2006**, *103*, 140–152. [CrossRef]

71. Zhang, N.; Zhang, X.; Yang, G.; Zhu, C.; Huo, L.; Feng, H. Assessment of defoliation during the Dendrolimus tabulaeformis tsai et liu disaster outbreak using UAV-based hyperspectral images. *Remote Sens. Environ.* **2018**, *217*, 323–339. [CrossRef]

72. Abdullah, H.; Darvishzadeh, R.; Skidmore, A.K.; Groen, T.A.; Heurich, M. European Spruce bark beetle (*Ips typographus*, L.) green attack affects foliar reflectance and biochemical properties. *Int. J. Appl. Earth Obs. Geoinf.* **2018**, *64*, 199–209. [CrossRef]